

STATUS REPORT ON SUSE *

W. Schott

Physik-Department, Technische Universität München, 8046 Garching, W-Germany

Abstract.- The design of the superconducting sector cyclotron SuSe for heavy ions in the whole mass range is in progress. The K-factor for the bending is $K_b = 1400$. The maximum energy is 450 MeV/n for protons and ^3He . For heavy ions with $q/A = 0.5$ and 0.16 ($^{238}\text{U}^{38+}$) 300 MeV/n and 21 MeV/n is obtained, respectively. The external beams have a high quality, e.g., for ^4He the energy spread should be $1.1 \cdot 10^{-4}$ at 23 ps pulse duration and a transverse emittance of 0.13π mm mrad. A full scale main coil is being constructed. RF-cavities for a very high accelerating voltage (≥ 1 MV) at the extraction radius have been developed. A power model will be built.

1. Introduction.- The design of the superconducting heavy ion sector cyclotron SuSe as a booster for the 13 MV Munich tandem is in progress. The characteristic features of the machine are established. A survey was already given in ref. 1. In Fig. 1 a plan view of SuSe is shown where the superconducting sector magnets, the RF cavities and the injection and extraction system are sketched. Some machine characteristics are listed in table 1. Data of typical beams are given in table 2.

At a large magnetic field level the superconducting sector coils behave like air coils because the iron is saturated. This causes a reverse field in a wide radial range between the sector magnets providing a large flutter and enough axial focussing for accelerating especially light ions to high energies. Only for protons the maximum energy T_2 ($T_2 = T(r_2)$) is determined by the focussing limit. Moreover, for protons and ^3He the $v_r = 2$ - stop band is nearly reached at T_2/A . For all other ions the largest T_2/A -value results from the maximum bending power of the guiding field. The final energy for one particular ion can be continuously lowered to at least half the value given in table 2 by reducing the field level.

The transverse emittances of the beams which are extracted from SuSe, are very small. This is due to the high quality of the tandem beams ($\approx 1 \pi$ mm mrad for the light ions), a proper matching and the adiabatic damping. The longitudinal ($\Delta T/T$, Δt)-phase space of the SuSe beams is also small. This is achieved by the small energy spread of the tandem beams and a well designed beam line connecting the tandem and SuSe which meets special requirements¹⁾ (focus in all three phase areas at the post stripper, "negative drift length" between post stripper and injection point, dispersion matching at the injection point, achromatic imaging between high energy buncher and post stripper, etc.). The resulting values for light

Table 1.- Machine data.

Injector	13 MV-tandem
Mean injection radius r_1	0.4 m
Mean extraction radius r_2	2.4 m
Mean field at r_2	2.23 T
Bending power K_b	1400
Iron weight per magnet	280 t
Particle revolution frequencies	14.7...4.2 MHz
2 accelerating cavities	TE 101 mode
RF frequency range	78.6...67.4 MHz
Harmonic operating modes h	5.,6.,7.,...16.
Maximum accelerating voltage per cavity	≥ 1 MV
Maximum RF power per cavity	100 kW
Beam separation $\Delta r(r_1)$	10 mm
beam separation $\Delta r(r_2)$	2.6 mm

ions at r_1 are $(\Delta T/T)_1 \approx 2 \cdot 10^{-3}$ and $\Delta t_1 \approx 100$ ps. $\Delta T/T$ is adiabatically damped in the cyclotron by an energy gain factor T_2/T_1 of about 62 for very light ions. Furthermore, the radially rising voltage distribution $U(r)$ of the cavities causes a shrinking of Δt by a factor which is given by $U(r_2)/U(r_1) \approx 4$. Although the energy spread of the particles in the center of the bunch is increased by the same factor, the total width ΔT of the phase area is smaller than in the case where a constant voltage is applied, as indicated in Fig. 2. Particles with a phase slip ωt are reduced in energy according to the $(1 - (\omega t)^2/2)$ -dependence of the accelerating voltage. Therefore, the bunches which are accelerated by a radially rising voltage are less distorted resulting in a smaller overall energy spread ΔT ²⁾. Single turn extraction and tight tolerances of the RF- and magnetic field are necessary to maintain the high beam quality. The accelerating voltage at r_2 is 2 MV/turn at maximum

* Supported by the German Ministry of Research and Technology.

Table 2.- Properties of some external SuSe beams. U_T means terminal voltage of the tandem, T/A energy per nucleon, ϵ emittance, Δt pulse width and I particle current. The index 2 indicates the values at r_2 , $(\Delta t)_{50m}$ corresponds to the pulse width at a distance of 50 m after extraction. The final currents I were obtained using standard tandem currents. For all beams which are heavier than magnesium -24 I is limited by the lifetime of the terminal stripper. The intensities are at maximum for the shown charge states where a terminal foil stripper at the voltage U_T and another foil stripper as a post stripper were taken into account.

Ion	U_T (MV)	T_2/A (MeV/n)	$(\epsilon_{r,z})_2$ (π mm mrad)	Δt_2 (ps)	$(\Delta T/T)_2$ (o/oo)	Δt_{50m} (ps)	I (pnA)
$^1_1\text{H}^+$	3.6	450	0.11	33	0.20	36	5000
$^3_2\text{He}^{2+}$	7.1	450	0.11	22	0.10	24	1000
$^4_2\text{He}^{2+}$	7.5	300	0.13	23	0.11	25	1000
$^{12}_6\text{C}^{6+}$	11.5	300	0.13	16	0.10	18	3700
$^{16}_8\text{O}^{8+}$	12.9	300	0.13	16	0.11	18	2000
$^{24}_{12}\text{Mg}^{11+}$	12.6	235	0.16	17	0.15	22	30
$^{23}_{16}\text{S}^{15+}$	13.0	246	0.16	17	0.17	25	18
$^{58}_{28}\text{Ni}^{21+}$	13.0	126	0.17	19	0.23	38	10
$^{81}_{35}\text{Br}^{26+}$	12.5	96	0.21	20	0.27	50	2
$^{127}_{53}\text{J}^{32+}$	12.9	56	0.28	26	0.30	74	1.3
$^{197}_{79}\text{Au}^{34+}$	11.9	25	0.41	46	0.31	120	1
$^{238}_{92}\text{U}^{38+}$	11.3	21	0.46	46	0.34	137	1

providing a beam separation $\Delta r(r_2)$ of several millimeters (cf. table 1). Therefore, the first requirement can be met. The stability of the RF-amplitude and frequency must be less than $4 \cdot 10^{-5}$ and 10^{-6} , respectively. The temporal relative deviations of the magnetic field are expected to be less than 10^{-6} (ref. 3).

In section 2 we report on magnet components and field construction, in section 3 the beam dynamics and the injection and extraction are sketched. In section 4 some technical aspects

of the magnets are described, especially the calculation of the magnetic forces on the superconducting coils and the resulting distortions and stresses. In section 5 the RF-system is outlined. Finally, a survey of the planned accelerator laboratory is given.

2. Magnet components and field construction.- The three-dimensional magnetic field calculations were done by means of the program GFUN3D.⁴⁾ Each magnet consists of two wide superconducting main coils and two superconducting coil layers, a C-shaped iron yoke and

a cold iron pole. In Fig. 3 horizontal and vertical sections of one magnet are drawn, schematically. In Fig. 4 a correcting layer is shown. By means of GFUN3D one sixteenth of the iron of one magnet is subdivided into elements within which the magnetization is assumed to be constant. With 205 yoke - and 40 pole elements the error of the magnetic field calculation is about one percent. One correcting coil is composed of several single coils. Geometrically each main- and single coil consists of six circular arcs. Fig. 5 shows the mean field of the whole magnet system which is produced by the main coils at different current levels with the iron poles and yokes present. Mean fields with iron poles and all iron removed are also shown. Thus, the mean field rise caused by the addition of iron is about twice as large as the mean field of the main coil itself. The iron contribution depends strongly non-linearly on the main coil current due to the more or less complete magnetization of the iron at different main coil currents. All iron of the magnets is assumed to be of the commercially available annealed soft

steel type⁵). Three correction field distributions must be produced independently by means of the coil layer:

a) For non-relativistic heavy ions the isochronous mean field is essentially constant. Therefore, the field must be increased close to the extreme radii r_1 and r_2 , in order to get a flat distribution \bar{B}_m in the whole radial range (cf. Fig. 5, curve a and b). This so called F-correction \bar{B}_{C3} is given at maximum main coil current i_1 by

$$\bar{B}_{C3}(i_1) = \bar{B}_m - \bar{B}(i_1),$$

where $\bar{B}_m = \text{const.}$

The F-correction at any main coil current i is given by $\bar{B}_{C3}(i_1)$ multiplied by a factor which makes it linearly dependent on i because $\bar{B}_{C3}(i)$ should for any i be small in comparison to the main coil contribution $\bar{B}(i)$. Furthermore, the factor must be such that \bar{B}_{C3} at the minimum main coil current i_2 is given by $\bar{B}_{C3}(i_2) = \bar{B}_{C3}(i_1)/s$, where s is a similarity parameter, $s = \text{const.}$ (cf. below). \bar{B}_{C3} is then given by

$$\bar{B}_{C3}(i) = \bar{B}_{C3}(i_1) \left(\frac{1-1/s}{i_1-i_2} (i-i_2) + \frac{1}{s} \right). \quad (1)$$

The above mentioned condition for $\bar{B}_{C3}(i_2)$ holds, as can be seen by setting $i = i_2$ in eq. (1).

b) The uncorrected field shape depends on the main coil current (cf. curve a and b of Fig. 5). This effect is due to the strongly non-linear behavior of the iron contribution (cf. Fig. 5, curve e and f) and must be corrected for by the coil layer. This contribution is called M-field \bar{B}_{C2} . In order to

apply the F-field at the minimum main coil current i_2 , $\bar{B}(i_2)$ must be corrected by $\bar{B}_{C2}(i_2)$ in such a way that the resulting field is similar to $\bar{B}(i_1)$, i.e., the condition $\bar{B}(i_2) + \bar{B}_{C2}(i_2) = \frac{1}{s} \cdot \bar{B}(i_1)$ with $s = \text{const.}$ must hold. $\bar{B}_{C2}(i_2)$ can be calculated from known fields by

$$\bar{B}_{C2}(i_2) = \left(\frac{k}{s} - 1 \right) \bar{B}_{C1}(i_2) + \frac{1}{s} \bar{B}_{Fe}(i_1) - \bar{B}_{Fe}(i_2),$$

where $k = i_1/i_2$.

The M-correction at any main coil current i is given by

$$\bar{B}_{C2}(i) = \bar{B}_{C2}(i_2) \frac{i_1 - i}{i_1 - i_2}.$$

This equation results from the linear dependence on i and from the condition $\bar{B}_{C2}(i_1) = 0$.

c) Finally, a radial rise of the mean field must be produced, e.g., $\Delta \bar{B}(r_2) = 0.58 \text{ T}$

for heavy ions with $q/A = 0.5$ and

$T_2/A = 300 \frac{\text{MeV}}{n}$. This so called R-contribution \bar{B}_{C4} is given by

$$\bar{B}_{C4} \approx \frac{B_0}{\sqrt{1 - \left(\frac{qB_0 c}{A E_u} r \right)^2}} - \bar{B}_m,$$

where B_0 is the field extrapolated to the machine center, E_u is the unit mass and c the speed of light.

\bar{B}_{C3} is difficult to produce because it is rather large at small radii ($\bar{B}_{C3}(r_1) \approx 0.25 \text{ T}$). This field correction requires the negatively curved coils of the correction layer⁶ (cf. Fig. 4 and 6). The R-field imposes the condition that with growing r more single coils must contribute to \bar{B}_{C4} . Therefore, the coils accumulate at the rear branch of the layer away from the machine center. The M-field turns out to be quite small ($\bar{B}_{C2} \approx 0.1 \text{ T}$) and depends on r only weakly. This correction field does not impose a special geometrical condition on the coil shape. It rather causes a slight modification of the coil currents as shown below. By means of an extended GFUN3D-program the mean field of the complete magnet system was fitted to the isochronous mean fields of heavy ions with extreme values of T_2/A and q/A . The currents were determined

as fit parameters. In Fig. 7 the produced mean isochronous fields for light ions with maximum and minimum T_2/A are drawn versus r . In Fig. 8 the current in the different coils of the layer is drawn for the two T_2/A values.

At high field level the current in coil # 1 is very large due to the F-correction. The R-field requires rather little current in all coils of the layer as can be deduced from Fig. 8, curve a. Actually, the R-correction is produced by subtracting field at small and adding field at large radii. This leads to a

slightly larger current in the main coil compared to the value which is noted in Fig. 5. Deviations of about 70 Gauss from the isochronous field with the period of 20 cm which are produced by correcting layers consisting of twelve single coils, yield too large phase shifts, especially, when very heavy ions are accelerated at high harmonic numbers (e.g., $h = 16$).⁷⁾ Calculations with a layer of twenty coils are being undertaken in order to reduce the absolute value and the period of the deviations. At low field level the current of coil # 1 is reduced due to a smaller F-correction. The currents in the coils # 3, 4 and 5 are enhanced because of the additional M-field \bar{B}_{C2} which must be produced at the main coil current i_2 . In Fig. 9 $B = \text{const}$ -curves for the large T_2/A -field are drawn. The field is reversed between the sector magnets yielding a large flutter factor F (cf. Fig. 10). The # 1 layer coil shapes the field between the magnets which can be seen from the negatively curved $B = \text{const}$ -lines. The valley has its largest depth and width at a radius $r \approx 1.6$ m which causes a maximum F value at this point. At low field level the current in the coils is smaller and the yoke iron is no longer saturated. The field between the magnets is slightly negative only for $r > 1.6$ m and positive for smaller radii. For very heavy ions at half maximum energy the field is positive in the whole radial range. Therefore, $F(r)$ is smooth and strongly reduced as can be seen from Fig. 10. curve b.

3. Beam dynamics, injection and extraction.-

The calculations on beam dynamics, injection and extraction are not completed yet. Large perturbing fields are necessary in order to inject the beam into the rather small first equilibrium orbit with radius $r_1 = 0.4$ m.

In Fig. 11 a possible injection system is sketched which uses superconducting septum magnets. These magnets can be mounted in cold connections between the superconducting correcting coils above and below the median plane. The outer stray field of the septum magnets causes a strong perturbation of the inner orbits of the cyclotron. This field is decreasing with opposite sign relative to the septum field. Its magnitude is about 25 percent of the inner field. By mounting dummy septum magnets at positions which are symmetrical to the machine center, a second field harmonic C_2 results which distorts

the inner orbits to a slightly oval shape. In an example which is shown in Fig. 11 the small radial beam width of ± 3 mm is conserved during the injection path between two magnets along a distance of 2.5 m. The axial beam width is kept to the same size by applying edge focusing at the curved septum magnet.

The orbit at radius r_1 is stable, if the equation⁸⁾

$$v_r - 1 > \frac{1}{2} \left| C_2 + \frac{1}{2} r_1 \left(\frac{dC_2}{dr} \right)_{r_1} \right| \quad (2)$$

holds, where C_2 is given by the Fourier expansion of the field

$$B = \bar{B}(r) \left[1 + \sum_n C_n(r) \cos n(\phi - \phi_n(r)) \right].$$

The right hand side of eq. (2) describes the width of the $v_r = 1$ - stop band which is

caused by the second harmonic field perturbation C_2 . According to eq. (2), $v_r - 1$ must be larger than this stop band width in order to obtain stable orbits in the injection region. In Fig. 12 the amplitudes $\tilde{C}_4(r)$ and $\tilde{C}_2(r)$ for one particular field ($q/A = 0.5$, $T_2/A = 300 \frac{\text{MeV}}{n}$) are drawn ($\tilde{C}_4 = \bar{B} C_4$, $\tilde{C}_2 = \bar{B} C_2$). The phase $\phi_2(r)$ of the second harmonic is also given. \tilde{C}_2 is large at $r \approx 0.3$ m because of the high inner fields of the septum magnets and falls off rapidly corresponding to a large index M ($M(r = 0.4 \text{ m}) = 5.3$, $M(r = 0.5 \text{ m}) = 4.7$)

where $C_2(r) \propto r^{-M}$. Numerical beam dynamical calculations which were done by means of the program FIXPO⁹⁾ using the above mentioned field, yield unstable inner orbits up to a radius of $r \approx 0.47$ m. Correspondingly, for $r \leq 0.47$ m the right side of eq. (2) is larger than the left side when the $\tilde{C}_2(r)$ -values of Fig. 12 are taken into account. The value of \tilde{C}_2 at r_1 of $\tilde{C}_2(0.4 \text{ m}) = 0.15$ T

at the given M produces a too large stop band width which leads to instability. There are two possibilities to meet the condition of eq. (2) in the radial range between 0.40 m and 0.47 m: Either M is changed in such a way that $|C_2 + 1/2 r_1 (dC_2/dr)_{r_1}|$ becomes small, or C_2 is reduced. ϕ_2 changes rapidly with increasing radius in the center region because, alternately, first the stray field, the inner field and again the stray field of the septum magnets contribute to the second harmonic. After reaching the outer boundary of the septum magnets at $r \approx 0.35$ m $2\phi_2$ remains constant being $2\phi_2 = 150^\circ$. This leads to a second harmonic of the form $\tilde{C}_2 \cos(2\phi - 150^\circ) = -\tilde{C}_2 \cos 2(\phi + 15^\circ)$.

Correspondingly, the second harmonic field perturbation for $r > r_1$ can be completely compensated for by means of another four superconducting coils which are mounted at the corners of a rhomb inside the orbit with $r = r_1$. The axes of the rhomb are shifted against the x- and y-axes by -15° (cf. Fig. 11). The coils must produce a second harmonic with the amplitude $\tilde{C}_2(r)$ of Fig. 12, b for $r > r_1$ and the sign reversed, i.e., $2\phi_2 = -30^\circ$. This can be done by four simple cylindrical coils. Each two coils which are

mirror reflected to the machine center, are identical and have the same current. The sign of the current is opposite to that in the neighboring septum magnet. An active or inactive channel along the 2.5 m long input trajectory seems to be necessary, especially for the very heavy ions at minimum final energy. This channel must be mirror reflected to the machine center, and the resulting second harmonic field can be included in the field analysis and compensated by the same device at least in the central region. At larger radii \tilde{C}_2 does not need to be completely cancelled because v_r is far from $v_r = 1$. In Fig. 12 c and d the isochronous mean field, v_r and v_z are drawn versus r for the field which was analysed in Fig. 12 a and b. The corresponding (v_r, v_z) diagram is shown in Fig. 13. The sum resonance $v_r + v_z = 2$ is crossed only once at a radius $r = 0.74$ m. At larger radii the $v_z(v_r)$ - curve is above the sum resonance. The loop in the $v_z(v_r)$ -curve is caused by the special field shape which was discussed in Fig. 9 and 10.

Because magnetic channels have fringe fields that shift orbit centers, it is useful to find an extraction solution that occupies $< 1/3$ of the orbit circumference. This minimizes the number of movable elements to fit the beam path close to the extraction trajectory. It seems possible to extract with one electrostatic and three magnetic elements as follows⁷⁾ (cf. Fig. 1): By means of D_2 in the valley a deflection of $\Delta\theta = 11$ mrad is achieved. At the position of the small magnetic channel in the second half of the next hill the separation will be 2 cm. The big channel in the first half of the following hill will be 15 cm beyond the circulating beam in a high gradient region. Finally the beam will be bent with a radius of curvature of $\rho = 3$ m to pass the yoke. By a proper geometry of the channel windings dB/dr and d^2B/dr^2 will be zero in S_5 and the fringe field is reduced to about 2 % of the inner value. In S_6 d^2B/dr^2 is zero.⁷⁾ The data for the deflecting elements is: $E_{D2} = 10$ MV/m, $B_{S5} = -0.4$ T, $B_{S6} = -0.7$ T, $dB_{S6}/dr = 0.1$ T/cm, $B_M = -1.8$ T.

4. Magnet technique. - Some details on the coil technique, as the construction of the windings, the cooling, the conductor and the quench protection were already described in refs. 1 and 10. A short sample of the conductor which was designed for a critical current of 3420 A at 7 T and 4.5 K, actually reached 4300 A at 7 T and 4.5 K during the test. A superconducting main coil of full size is being manufactured¹¹⁾. The photo (Fig. 14) shows the coil bobbin

which was made from a special aluminium cast. The complete coil will be delivered in November 1981 and will be tested in a recently established test laboratory at our accelerator facility. The maximum tolerable stress of the aluminium cast was measured to be $2.2 \cdot 10^8$ N/m².

The magnetic forces and the resulting distortions and stresses have been calculated by means of the finite element-method using the program SAPV¹²⁾ for the main coil and the correcting layer. The results which are discussed in detail in ref. 13, will be reviewed briefly. Fig. 15 shows a horizontal cross section of one half of the main coil which is subdivided into finite elements. By choosing rectangular elements and a proper numbering the errors for the stress calculation are a few per cent. The coil consists of four plates which are extended in the (x,y) -plane. They are 2.75 cm thick and have an axial distance of 8.5 cm from each other. Between these plates are three winding sections. The windings are fixed by metallic bands which surround the frame at the circumference. From symmetry reasons it is sufficient to subdivide only one half of the coil. The second half is taken into account by setting the degree of freedom for the nodal point motion in y -direction in the $y = 0$ -plane equal to zero. The distortions depend on the specific suspension of the coil. The fixpoints are symbolized by the supports a to d. The magnetic field B in the center of the current carrying winding elements was calculated by means of GFUN3D taking all four SuSe magnets at the highest field level (cf. Fig. 7a) into account. In Fig. 16 the components of the forces are drawn for the different current elements along the coil windings in the three sections. F_x distorts the coil at small radii towards the machine center and at large radii away from the center. The sum over all F_x -components yields a radially outward directed force of $1.64 \cdot 10^6$ N. F_y is always positive and is taken up by the coil frame. F_z is positive in plane a, decreases with increasing z and is negative in plane c. Thus, the coil is axially compressed. The absolute value of F_z is larger in c than in a. Therefore, there remains a resulting force which acts towards the plane $z = 0$ which must be taken up by the supports c, d and b. The modul of elasticity E for the aluminium cast coil frame and the niobium titanium-copper winding was taken to be $8 \cdot 10^{10}$ N/m² and $4 \cdot 10^{10}$ N/m², respectively. The E -value for the winding is low because of the potting by epoxy. The shearing modul G is given by $G = E/2(1+\nu)$, where ν is taken to be $\nu = 0.3$. The coil structure is widened by about 0.5 mm at the rear away from the machine center and axially bent by about 0.2 mm. In this calculation the large holes in the coil frame for inserting the iron of the pole (cf. Fig. 14) were not taken into account. By means of SAPV the six independent stress components in each finite element are calcu-

lated. The stress σ_{eq} follows from these components by¹⁴

$$\sigma_{eq} = [\sigma_x^2 + \sigma_y^2 + \sigma_z^2 - \sigma_x \sigma_y - \sigma_y \sigma_z - \sigma_z \sigma_x + 3(\tau_{xy}^2 + \tau_{yz}^2 + \tau_{zx}^2)]^{1/2}.$$

σ_{eq} is a good quantity to describe the actual straining of the material and can be compared with the maximum tolerable stress. σ_{eq} of the main coil turns out to be $7 \cdot 10^7$ N/m² at maximum which is by a factor of three less than the limiting value which was mentioned above.

The current at maximum field level in coil # 1 of the correcting layer is 573.000 A turns. This is about ten times as large as the current in the other single coils. Therefore, only coil # 1 has been taken into account in the finite element analysis of the correcting layer. Fig. 17 shows a horizontal cross section of one half of the correcting layer. It consists of the winding which has an axial height of 12 cm. At the bottom and top there is a plate of thickness 1 cm. At the circumference of the coil there is, similar to the main coil, a metallic band to take up the radial forces. The band is widened giving the correcting layer the same shape as the main coil in the (x,y) plane. At the band the layer is fixed axially to the main coil. Furthermore, radial supports a and b at the rear are provided. Fig. 18 shows the force components acting on coil # 1. F_z is negative at the rear and positive close to the machine center. The sum of the F_x -components over all elements yields a radial force of $-1.22 \cdot 10^6$ N which acts towards the machine center and cancels nearly the outward directed force on the main coil. Thus, only a force of $0.42 \cdot 10^6$ N must be taken up by the radial supports of the main coil and the layer at maximum current in both coils. The winding- and frame material was assumed to be the same as for the main coil. The layer is widened at the circumference by about 0.8 mm. σ_{eq} is 10^8 N/m² at maximum which is a factor of two smaller than the limit. The detailed design of the magnet and the vacuum chamber which also takes into account the magnetic pressure on the yoke ($3 \cdot 10^6$ N/m², ref. 7) is being undertaken.

5. RF-System.- The RF-system is described in ref. 15 in detail. In Fig. 19 one of the two cavities (cf. Fig. 1) is shown schematically. Its radial and axial dimension is 3 m and 2.4 m, respectively. The width is 2 m at maximum. The horizontal cross section is widened in the machine center in order to provide room for the RF-magnetic flux, thus, rising the accelerating voltage at the injection radius. The frequency variation between $\nu = 78.6$ MHz and $\nu = 67.4$ MHz is

done by increasing the capacity in reducing the angular width $2\Delta\phi$ of the accelerating gap successively. The fine tuning of $\Delta\nu = \pm 0.5$ MHz is done by changing the inductance with two cylindrical perturbing objects. The cavity is driven in the TE 101-mode, i.e., at both ends of the radial resonator width the voltage is zero and there is a maximum in between. The radial dimension has been optimized in order to obtain the maximum voltage at $x_2 = 2.18$ m (cf. Fig. 20). x_2 is the radial coordinate of the extraction orbit with mean radius r_2 . The horizontal cross section, which is given in Fig. 20, is determined by the shape of the main coils. Apart from the accelerating gap width the resonant frequency ν is given by the axial height of the cavity. ν and the shunt impedance R_s increase with decreasing height as was already discussed in ref. 1., suggesting to make the axial dimension as small as possible and using high RF frequencies and harmonic numbers h . The lower limit of the cavity height is obtained by the maximum harmonic number ($h = 16$) which can be used at given field errors, i.e., deviations from the isochronous field. The ν -range has been chosen in such a way that at the upper limit fully stripped light ions ($q/A = 0.5$, $T_2/A = 300$ MeV/n, cyclotron frequency $\nu_0 = 13.1$ MHz) are accelerated with $h = 6$ and a wide accelerating gap. The transit time factor is then 0.83. By shifting ν to the lower limit and using h -values up to $h = 16$ all cyclotron frequencies from 13.1 MHz down to 4.2 MHz, which corresponds to ν_0 for $q/A = 0.16$, $T_2/A = 21$ MeV/n, are covered. Thus, with this scheme the very heavy ions as $^{197}\text{Au}^{34+}$ and $^{238}\text{U}^{38}$ can be accelerated only to their maximum energy. Their half maximum final energy, which is considered to be of little importance for SuSe, would require an extended ν -range down to 49.6 MHz. Protons and ^3He which have the highest ν_0 at maximum energy of $\nu_0 = 14.7$ MHz, are accelerated with $h = 5$. In order to achieve a beam separation of $\Delta r = 2.6$ mm at the extraction radius r_2 , a maximum cavity voltage of $U_0(r_2) = 1.3$ MV is required for ^3He with a final energy of $T_2/A = 450$ MeV/n. For all other heavy ions $U_0(r_2) = 1$ MV and less is needed. It might be possible to reduce the large U_0 -value for ^3He by precessional extraction. The resonator has been optimized by means of the recently developed program CAV3D¹⁶⁾. With CAV3D the three-dimensional cavity volume is approximated by a spatial grid consisting of cubes with fixed size. At each cube center the field components H_x , H_y and H_z are calculated. The subdivision into cubes of a minimum size is indicated in the horizontal and vertical cross section of the cavity in Fig. 20. The relative errors for determining the frequency, voltage and shunt

impedance are 1 %, 10 % and 20 %, respectively, as could be deduced by comparing the numerical values with measurements which were done using a 1:5 model resonator (cf. Fig. 21). In Fig. 22 the shunt impedance R_s and the accelerating gap width $\Delta\phi$ versus v^S are shown. The RF-power P which is necessary to accelerate the various heavy ions to different final energies, can be calculated from the required $U_0(r_2)$ -values using the $R_s(v)$ - and $\Delta\phi(v)$ -curves and taking the transit time factor into account. In Fig. 23 P for several ions is drawn.

6. Outline of the new laboratory.- In Fig.24 a plan view and a vertical section of the planned accelerator laboratory is shown. SuSe is integrated into the left part of a new building which is 97 m long, 26 m wide and 9 m high. At the site of the cyclotron and a large magnet spectrograph the height is increased to 12 m and 15 m, respectively. The accelerated heavy ions having passed the tandem and SuSe are guided to several experimental set ups in the new hall. A large scattering chamber, a mass separator for the production of secondary exotic beams, a pion spectrometer and a large magnet spectrograph with a high resolution ($\Delta T/T = 3 \cdot 10^{-5}$) for nuclear structure experiments have been planned.¹⁷⁾

References.-

1. H. Daniel et al., IEEE Trans. on Nucl. Science, NS-28 (1981) 2107.
2. W. Joho, Part. Accel. 6 (1974) 41 and G. Hinderer, Internal Report, Technische Universität München (June 1980), unpublished.
3. G. Hinderer, Internal Report, Technische Universität München (April 1981), unpublished.
4. A. G. A. M. Armstrong et al., Report RL-76-029/A, Rutherford Laboratory (1976), unpublished.
5. Friedr. Krupp GmbH, Krupp Widia, HyperMO, Essen (1980). Thyssen Heinrichshütte AG, ZSH-Spezial, Hattingen (1980).
6. W. Schott, E. Zech, Internal Report, Technische Universität München (June 1980), unpublished.
7. R. E. Pollock, Internal Report, Technische Universität München (May 1981), unpublished.
8. W. M. Schulte, The Theory of Accelerated Particles in AVF Cyclotrons, Thesis, Berlin (1978), unpublished.
9. W. Joho, G. Rudolf, Program FIXPO, SIN, Villigen (1975), and H. J. Scheerer, private communication.
10. U. Trinks, Internal Report, Technische Universität München (October 1979), unpublished.
11. Brown, Boveri and Cie. (Mannheim, Germany).
12. K. J. Bathe, E. L. Wilson, F.E. Petersen, Report EERC 73-11, Berkeley (1973, revised 1974), unpublished.
13. W. Schott, Internal Report, Technische Universität München (February 1981), unpublished.
14. S. P. Timoshenko, N. J. Goodier, Theory of Elasticity, 2. ed., McGraw-Hill, New York (1951).
15. W. Wilhelm, E. Jaeschke, Internal Report, Technische Universität München (July 1981), unpublished.
16. W. Wilhelm, Program CAV3D, Technische Universität München (1981).
17. P. Kienle, Internal Report, Technische Universität München (July 1980), unpublished.

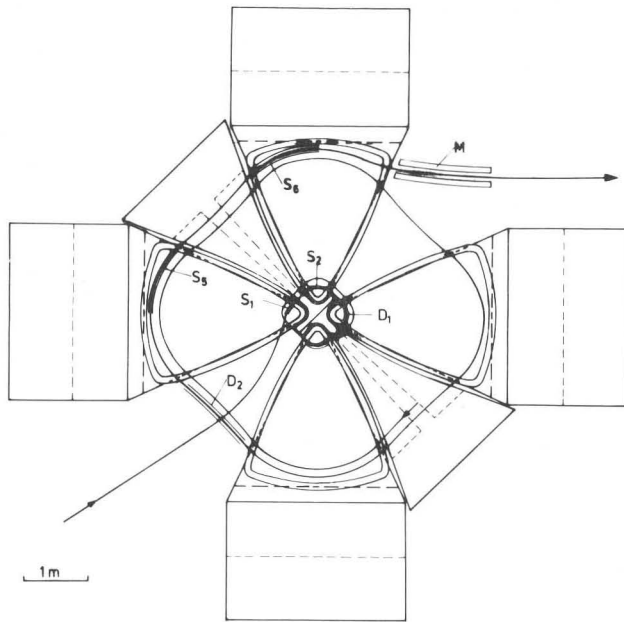


Fig. 1 : Plan view of SuSe. D means electrostatic deflector, S septum magnet, M Magnet.

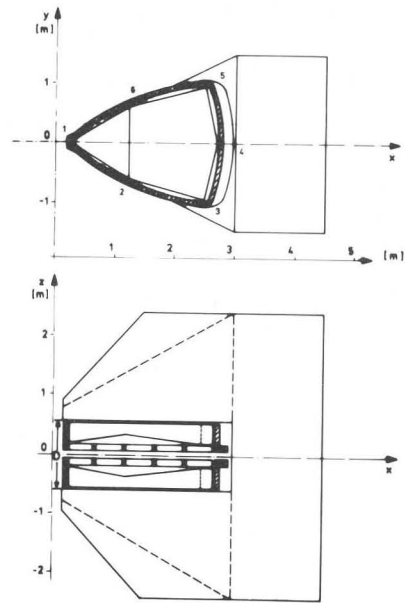


Fig. 3 : Plan view and vertical section of a SuSe-magnet.

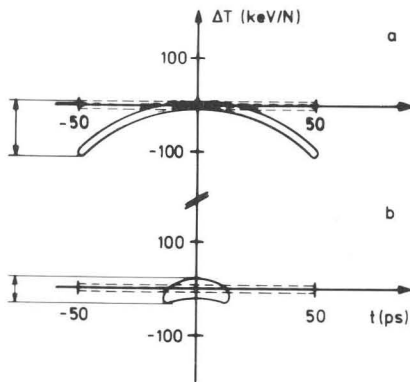


Fig. 2 : Invariant longitudinal phase area for ${}^4\text{He}$ at the injection radius r_1 (dashed line) and at the extraction radius r_2 (drawn line). a) accelerating voltage $U = \text{const.}$ b) $U(r_2) / U(r_1) = 4.$

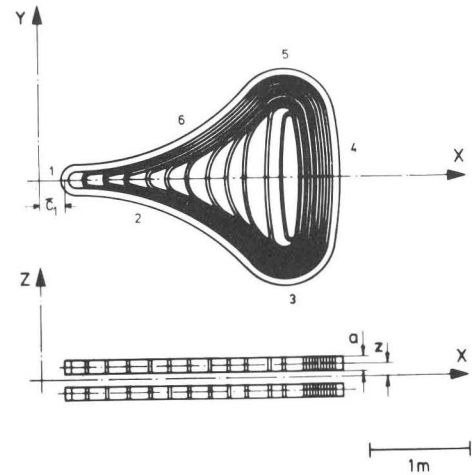


Fig. 4 : Cross sections through the correcting coil layer.

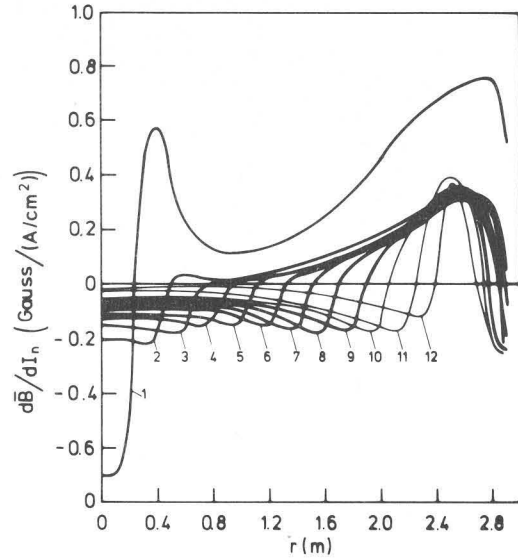
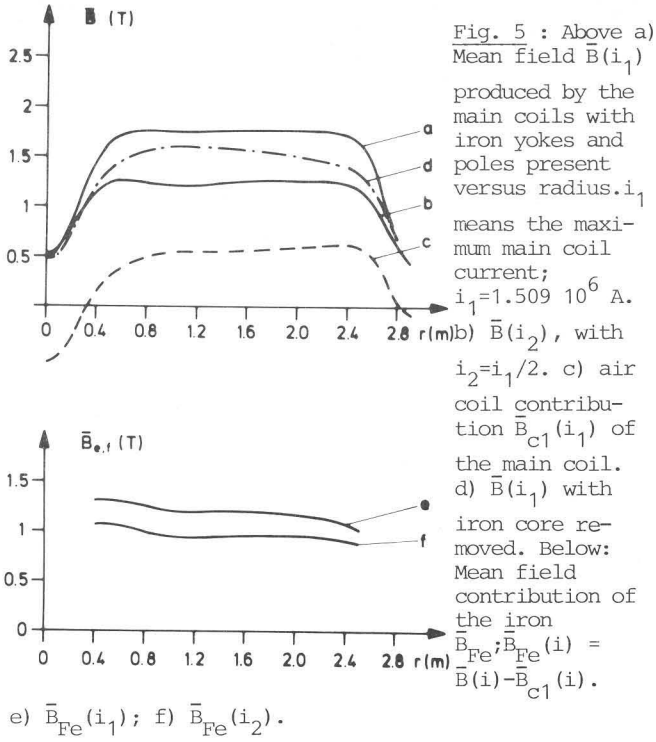


Fig. 6 : Mean field contributions of layer coils to \bar{B} for $q/A = 0.5$, $T_2/A = 300$ MeV/n versus radius; # 1 corresponds to the largest coil etc.

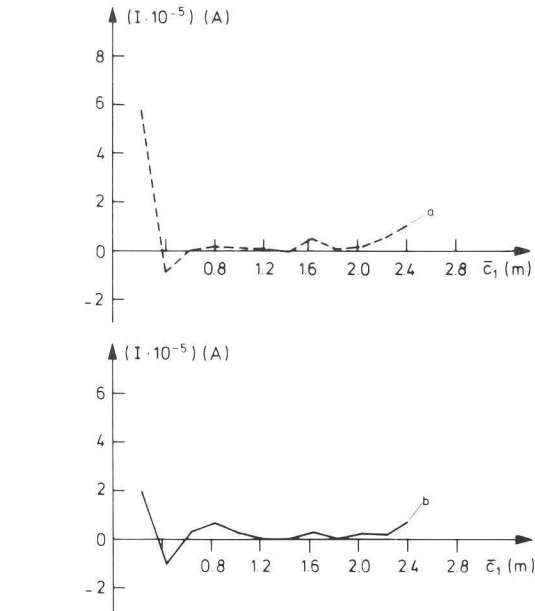


Fig. 8 : Currents in different layer coils at \bar{B} for $q/A = 0.5$ versus \bar{c}_1 . \bar{c}_1 denotes minimum distance of coil to machine center. a) $T_2/A = 300$ MeV/n, $i_1 = 1.85 \cdot 10^6$ A, current density in coil # 1 $J_1 = 8400$ A/cm², in main coil $j_{mc} = 10408$ A/cm². b) $T_2/A = 150$ MeV/n.

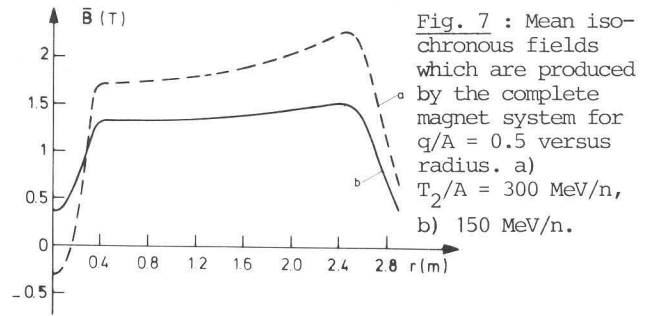


Fig. 7 : Mean isochronous fields which are produced by the complete magnet system for $q/A = 0.5$ versus radius. a) $T_2/A = 300$ MeV/n, b) 150 MeV/n.

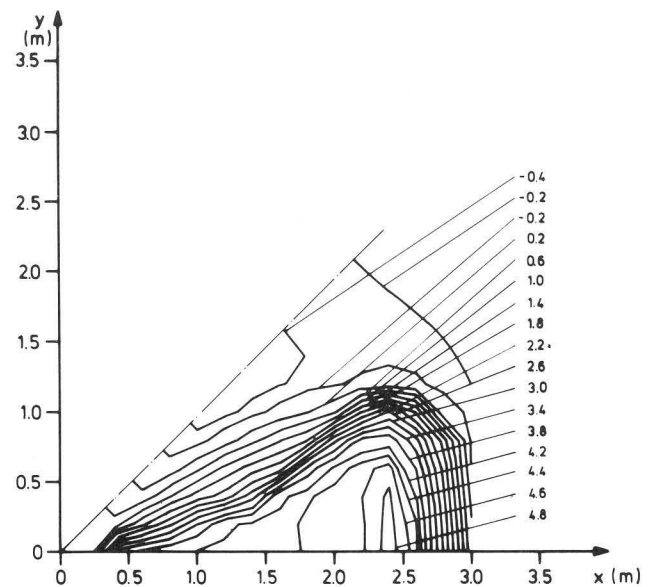


Fig. 9 : Curves $B = \text{const}$ in the (x,y) plane, B -values in Tesla; field as Fig. 7a.

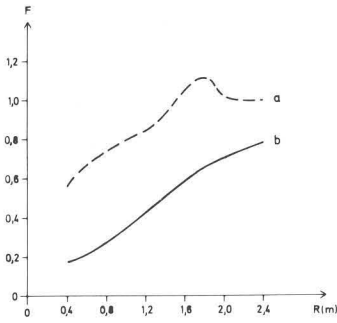


Fig. 10 : Flutter factor versus radius. a and b as Fig. 7a,b.

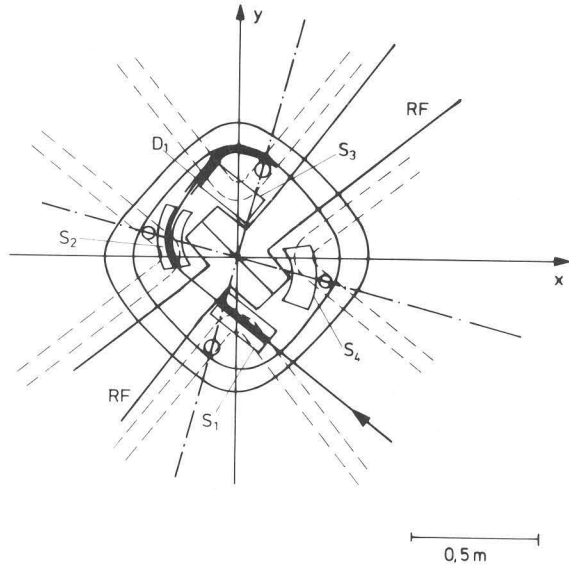


Fig. 11 : Injection system using two superconducting septum magnets S_1 , S_2 and an electrostatic deflector D_1 . For $q/A = 0.5$, $T_2/A = 300$ MeV/n the fields of S_1 , S_2 and D_1 are $B_{S1} = -1.5$ T, $B_{S2} = 2$ T and $E_{D1} = 15$ MV/m. S_3 and S_4 are dummy septum magnets with the same fields as S_1 and S_2 . They are mounted symmetrically to the machine center. The inner orbit with $r = 0.4$ m is unstable due to the second harmonic of $S_1 \dots S_4$. The outer orbit ($r = 0.49$ m) is stable. The second harmonic is compensated by the four cylindrical coils.

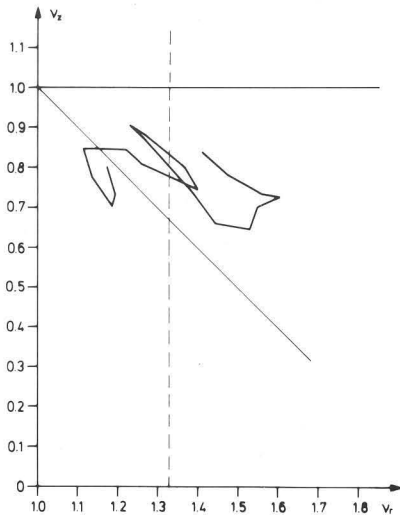


Fig. 13 : Tune diagram of the field of Fig. 7,a.

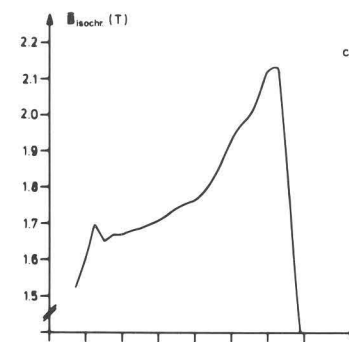
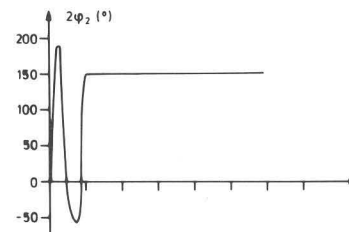
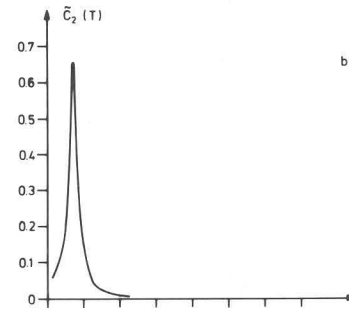
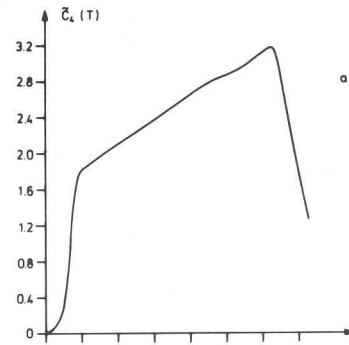


Fig. 12 : Radial distributions corresponding to the analysis of the field of Fig. 7,a. a) Fourth harmonic, b) second harmonic and phase angle, c) mean isochronous field, d) ν_r and ν_z for $r \geq 0.49$ m.

field, d) ν_r and ν_z for $r \geq 0.49$ m.

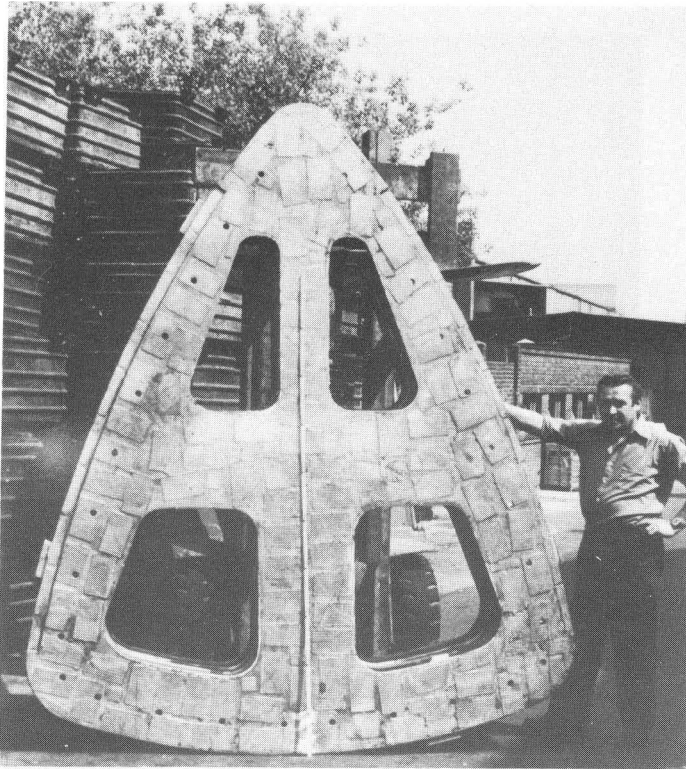


Fig. 14 : Casting of main coil frame of 1:1 test coil.

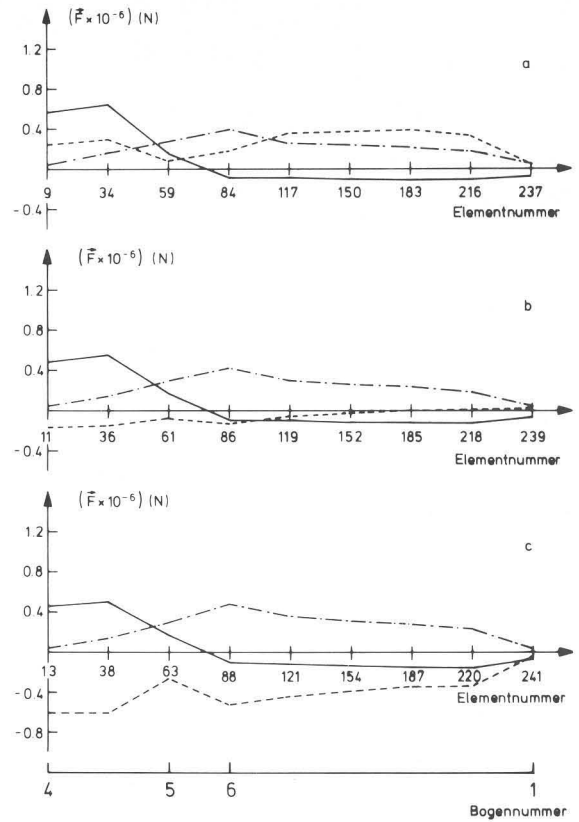


Fig. 16: Force components on current elements along the three winding sections of the main coil from the rear towards the machine center. a) bottom section (close to particle plane), b) middle, c) top. Drawn line: F_x , dash-dotted: F_y , dashed: F_z .

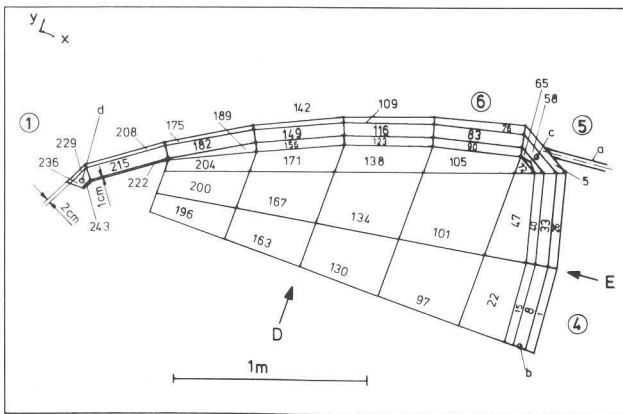


Fig. 15 : Horizontal cross section through the bottom plate of one half of the main coil which is divided into finite elements for the stress calculation.

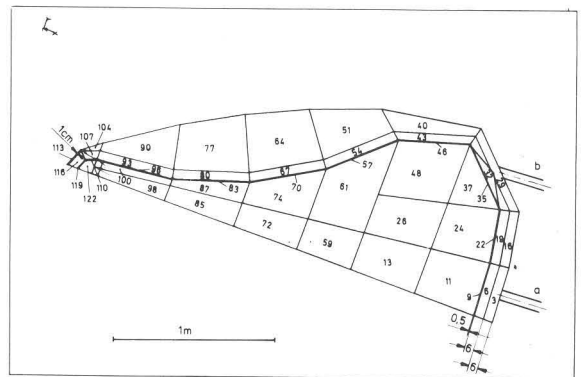


Fig. 17 : Horizontal cross section through the top plate of one half of the correcting coil layer.

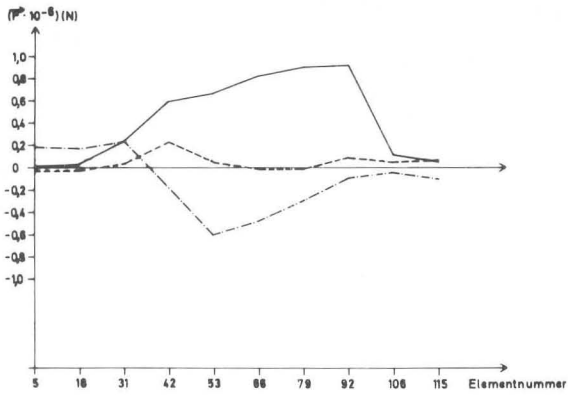


Fig. 18 : Force components along the coil # 1 of the layer. Dash-dotted line: F_x , drawn: F_y , dashed: F_z .

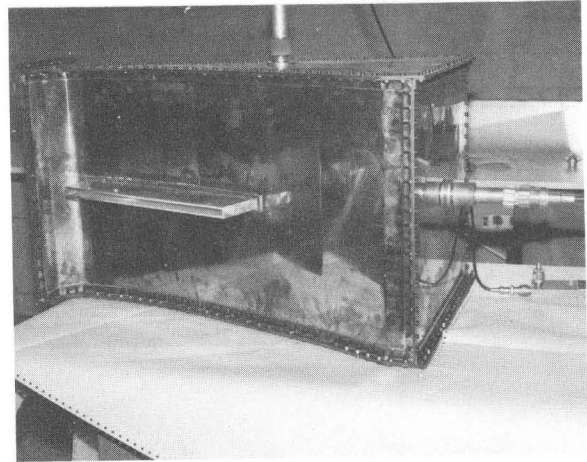


Fig. 21 : 1:5 model-resonator

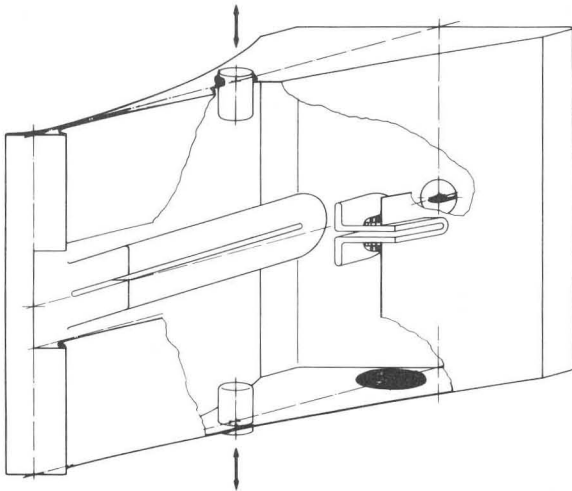


Fig. 19 : RF-cavity, schematically.

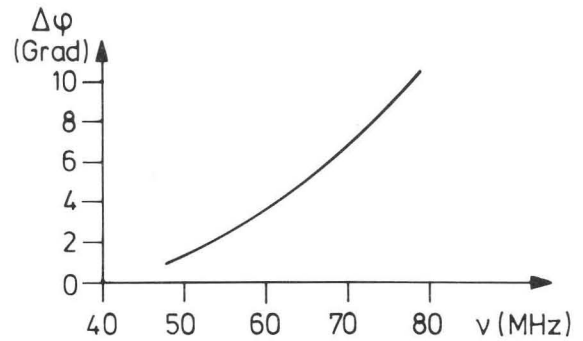
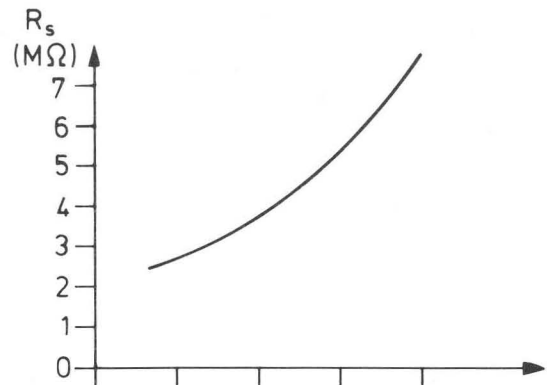


Fig. 22 : Shunt impedance R_s and gap width $\Delta\phi$ versus RF-frequency ν of the cavity.

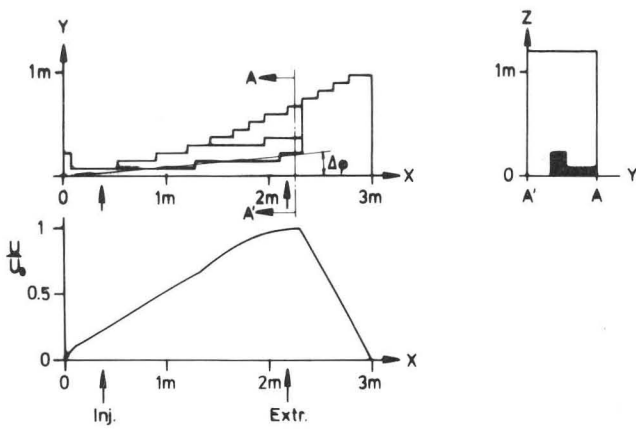


Fig. 20 : Representation of the cavity contours by a grid as it is used for calculations with CAV3D. Above: Horizontal and vertical cross section halves, below: voltage distribution.

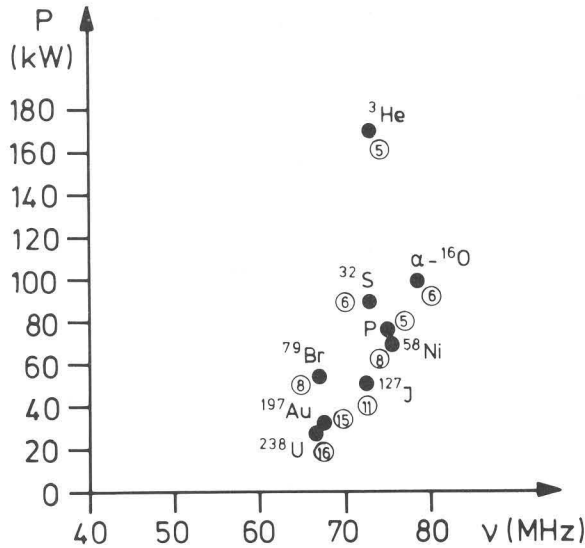


Fig. 23 : Power loss P in the cavity versus ν for accelerating different heavy ions to the maximum final energy. The numbers in circles denote harmonic numbers.

" DISCUSSION "

H.G. BLOSSER : Does the prototype sector which you are building include the correcting coils ?

Will you also build a prototype structure for the correcting coils ?

W. SCHOTT : No, the construction of the correcting coil layer will be the second step.

After having learned the technology with the main coil, we most probably will build a full size correcting coil layer where we want to apply the same technique, i.e. a conductor of the same type and a similar construction principle of the layer frame.

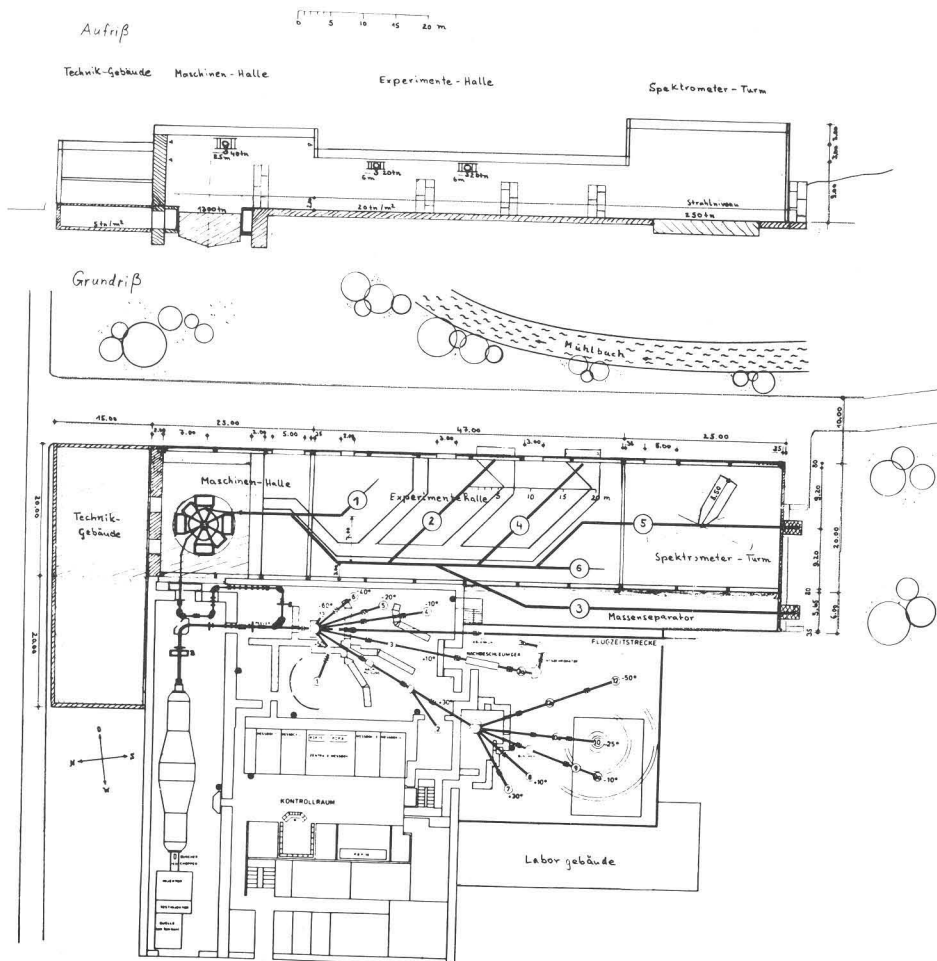


Fig. 24 : Plan view and vertical section of the laboratory. East of the existing tandem laboratory a new building is planned which will contain SuSe and experimental facilities.